Nanoscale

PAPER

View Article Online
View Journal

Cite this: DOI: 10.1039/d6nr00807k

Nanoscale thermocapillary flow as a recording medium for infrared absorption spectra of individual carbon nanotubes

Kai Watanabe, [a] Shigeo Maruyama [a,b,c] and Keigo Otsuka *[a]

Received 26th February 2026,
Accepted 21st April 2026

DOI: 10.1039/d6nr00807k

rsc.li/nanoscale

Thermally induced deformations of polymer thin films are fundamental to high-resolution thermal lithography and thermal property characterization. Among various heating methods, laser-induced thermocapillary flows convert nanoscale localized heating into surface deformation, providing a non-contact strategy for the selective removal of metallic carbon nanotubes (CNTs). Although chirality-dependent optical responses can be exploited for bandgap-selective removal of CNTs, detailed optical spectra of CNTs supported on substrates remain difficult to obtain because of their extremely small volumes and pronounced environmental influences, including doping and dielectric screening. Here, we utilize laser-induced nanoscale thermocapillary flows as a photothermal probe to visualize the near-infrared absorption response of an individual CNT on a substrate. The CNT is irradiated with a wavelength-tunable near-infrared laser (1100–1500 nm), and the wavelength dependence of the resulting trench depth in the polymer film is analysed to extract the optical response recorded in the thin film. The measured trench profile exhibits an unexpected reduction in the photothermal response above 1400 nm. We demonstrate that this behaviour does not directly represent the intrinsic absorption spectrum of the CNT. Thermofluidic simulations that incorporate the temperature dependence of polymer viscosity reveal a nonlinear amplification of trench formation under pulsed heating. After accounting for these nonlinear effects, spectral features corresponding to the exciton state and phonon sidebands are reconstructed. These findings establish thermocapillary deformations as a quantitative nanoscale photothermal spectroscopy method and provide a framework for evaluating environment-dependent optical spectra, with implications for chirality-selective CNT processing as well as high-resolution and rapid thermal patterning.

Introduction

Thermally induced deformations of polymer thin films have become a key microfabrication approach for high-resolution thermal lithography and nanoscale patterning.[1] When subjected to heating, polymer films exhibit several coupled responses, including thermal expansion, viscous flow, and material removal. The resulting deformation is strongly governed by the material properties and spatial temperature gradients. Such thermally driven deformations have been applied to visualize laser-induced localized heating, enabling the measurement of thermal properties of substrates,[2] thin films,[3] and graphene.[4] This approach can be extended to one-dimensional nanomaterials such as carbon nanotubes (CNTs). In addition, the highly localized deformation of thin films has been employed for nanoscale fabrications[5] and device processing.[6,7]

Among various deformation mechanisms, thermocapillary flows arising from temperature-dependent surface tension gradients have attracted considerable interest as an effective means of converting the localized heating into nanoscale surface topography. This mechanism has been applied to selective removal of metallic (m-) CNTs based on differences in their electrical conductivity[8,9] and optical absorption.[10] In these methods, mid-infrared laser irradiation preferentially heats m-CNTs beneath an organic thin film, creating steep local temperature gradients that induce Marangoni convection. The resulting nanoscale trenches function as self-aligned masks for subsequent plasma etching, enabling metallicity-selective purification of CNT arrays directly on insulating substrates.

Beyond the Drude-like absorption in the mid-infrared region,[11] CNTs exhibit a variety of optical features, including subband excitonic resonances, non-resonant continuum

---

[a] Department of Mechanical Engineering, The University of Tokyo, Tokyo, 113-8656, Japan. E-mail: otsuka@photon.t.u-tokyo.ac.jp
[b] School of Mechanical Engineering, Zhejiang University, Hangzhou, 310027, China
[c] Institute of Innovation for Future Society, Nagoya University, Nagoya, 464-0861, Japan

absorption, and phonon sidebands, which depend on their chirality.[12–14] Utilizing these spectral characteristics would enable extension of the method to diameter-selective purification. However, achieving bandgap-level selectivity requires a quantitative understanding of the optical absorption spectrum of an individual CNT under identical environmental conditions. Although absorption spectra have been reported for various chiral species of CNTs,[15–17] their optical response is highly sensitive to external factors such as doping,[18] strain,[19–22] bundling,[23,24] and dielectric screening.[25–31] In particular, excitonic resonances are strongly influenced by the surrounding environment. Redshifts have been observed in solvents,[32,33] under controlled atmosphere,[34,35] and on substrates.[28,36] For CNTs on substrates, substrate-induced dielectric screening,[28] strain,[19] and unintentional doping are considered to induce both red shifts and attenuations of optical transition peaks. These effects highlight the importance of performing measurements under realistic processing conditions. Although spectroscopy of individual CNTs has been demonstrated using photocurrent[37] and Rayleigh scattering,[38] the thermocapillary-flow-induced film deformation provides an alternative means to directly record the photothermal absorption under the same conditions used for device processing.

In this study, we reinterpret trench formation induced by thermocapillary flows not merely as a fabrication technique, but as a spectroscopic tool for visualizing the optical absorption of nanomaterials. By irradiating an individual CNT supported on a substrate with wavelength-tunable near-infrared light and examining the wavelength dependence of the resulting trench depth, we quantitatively evaluate the optical absorption. In addition, by incorporating the temperature dependence of polymer viscosity into thermofluidic simulations, we elucidate the nonlinear amplification mechanism of trench formation under pulsed heating. After correcting for this nonlinear contribution, the intrinsic absorption spectrum is reconstructed based on an established excitonic framework. This methodology enables quantitative photothermal spectroscopy of heterogeneous low-dimensional materials without elaborate fabrication processes and establishes a basis for advancing high-resolution thermal lithography based on localized photothermal conversion.

Results and discussion

Quantitative evaluation of trench morphology formed *via* thermocapillary flows

The selective removal of metallic CNTs is a critical requirement for the application of semiconducting CNTs in electronic devices. To avoid degradation of device performance, this process must proceed without introducing structural defects or damage to semiconducting CNTs. Du *et al.* reported the selective removal of metallic CNTs through nanoscale deformation of an organic thin film covering CNT arrays, followed by etching of the locally exposed CNTs.[10] The observed deformation of the viscous organic film was attributed to thermally driven flows induced by laser heating of CNTs. When a CNT embedded beneath an organic thin film on a substrate is heated, heat diffuses toward the film surface, establishing a temperature profile with a maximum directly above the CNT (Fig. 1a). The resulting temperature gradient induces a spatial variation in surface tension, which drives thermocapillary flows at the film surface. Consequently, the thin film undergoes localized deformation above the CNT, forming a trench structure. In this study, we first perform a quantitative assessment of the morphology of trenches formed by thermocapillary flows.

To investigate trench formation induced by laser heating of an individual CNT in detail, we prepared arrays of aligned and spatially isolated CNTs. This configuration minimizes thermal interaction between neighbouring CNTs and allows the trench formation process to be attributed to a single CNT. CNTs were synthesized using alcohol catalytic chemical vapor deposition with an iron catalyst deposited on a single-crystalline quartz substrate (Fig. 1b). A thin organic layer was subsequently deposited by spin coating a 1 wt% poly(methyl methacrylate) (PMMA) solution in anisole. The PMMA film thickness was measured by atomic force microscopy (AFM) to be 24 nm (Fig. S1). The same samples were later used for absorption spectroscopy measurements based on laser-induced trench formation.

Trenches were formed by scanning a laser beam perpendicular to the CNT axis at a speed of 1 μm h^{-1}. A nanosecond pulsed supercontinuum laser (SuperK COMPACT, NKT Photonics), covering a spectral range of 400–2400 nm, was employed, and the desired wavelength range was selected using a bandpass filter with a bandwidth of 50 nm (Fig. S2b). To promote thermocapillary flows, the sample was mounted on a heater maintained at 100 °C during irradiation. Fig. 1c presents an AFM image of a representative trench formed on the thin-film surface together with the corresponding cross-sectional profile at its deepest point. The trench was formed

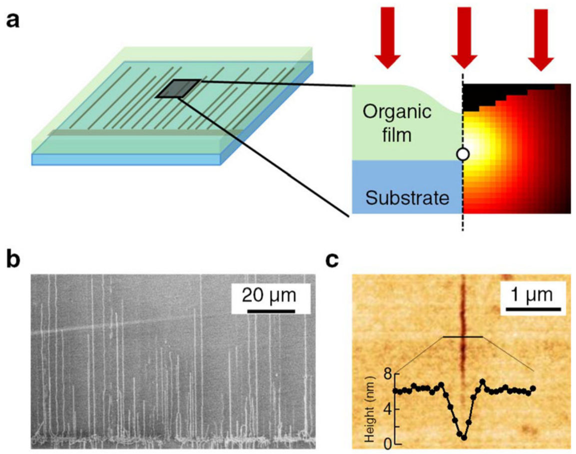

Fig. 1 (a) Schematic of a sample consisting of horizontally aligned CNTs covered with an organic thin film. (b) SEM image of as-grown SWCNT arrays. (c) AFM image and cross-sectional profile around a trench formed through laser-induced thermocapillary flow.

directly above the CNT, with a depth of several nanometres and a width of approximately 100 nm. The trench depth was smaller than the PMMA film thickness, indicating that the CNT remains fully covered and is not exposed to air. The trench depth was defined as the difference between the average film height away from the trench and the minimum height at the trench bottom (inset of Fig. 1c). Repeated AFM measurements after laser irradiation confirmed that the trench morphology did not change, demonstrating that the deformation is irreversible at room temperature. This irreversibility indicates that trench formation arises from localized thermocapillary flows driven by the temperature gradient generated through laser heating of the CNT.

Because deformation of the polymer thin film is irreversible, the resulting trench geometry preserves the time-integrated heat generation within the CNT arising from optical absorption of the incident laser. As schematically shown in Fig. 2a, trenches formed at different positions along an isolated CNT while varying the laser wavelength encode the wavelength dependence of optical absorption in their morphology. In this framework, the trench geometry serves as a measurable proxy for the optical absorption strength of the CNT. Fig. 2d presents a series of AFM images of trenches produced above a single CNT on a quartz substrate under different irradiation wavelengths. The corresponding trench depth profiles along the CNT axis are shown in Fig. 2e. The trench depth exhibits a spatial distribution along the tube axis, and the width and magnitude of this distribution varies with irradiation conditions. These variations originate from the Gaussian-like intensity profile of the laser beam, thermal conduction along the CNT axis, and a mechanical drift of the sample stage on the order of 1 μm. To reduce the influence of these factors, we define the trench area as the integral of trench depth along the CNT axis. The trench area at each wavelength (Fig. 2f) reflects not only the wavelength-dependent optical absorption of the CNT but also the transmission characteristics of the objective lens in the optical system, which cause the incident laser power to vary with the centre wavelength (Fig. 2b).

Since the trench area is sensitive to the laser power under each irradiation condition, a quantitative comparison across wavelengths requires calibration to remove the wavelength dependence of the optical system. To examine the effect of input laser power on trench formation, we performed simulations based on the model proposed by Song *et al.*[39] In this model, heat generated within the CNT spreads through the thin film *via* thermal conduction, leading to a spatial temperature rise at the film surface, $\Delta T_{\mathrm{surface}}(x)$. The surface tension γ is assumed to vary linearly with temperature as $\gamma = \gamma_0 - \gamma_1 \Delta T_{\mathrm{surface}}(x)$, where γ_0 is the surface tension at $T = T_\infty$ and γ_1 is the temperature coefficient. This temperature-dependent surface tension produces a gradient along the film surface, driving thermocapillary flows. The resulting film deformation is described by the Navier–Stokes equations, assuming constant viscosity and density and neglecting inertial and body-

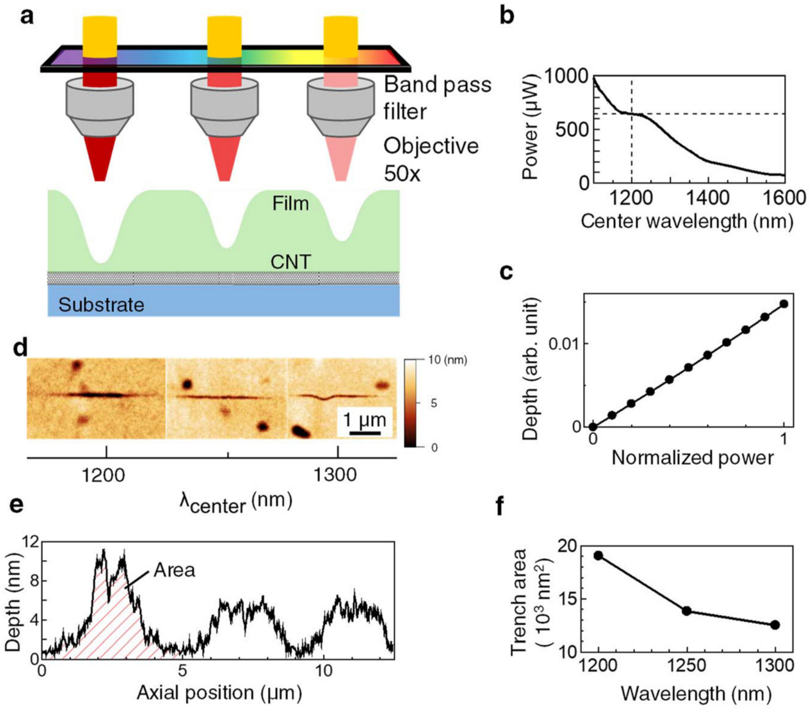

Fig. 2 (a) Schematic illustration of spectroscopy based on trench formation. (b) Wavelength dependence of the laser power exposed to the sample. Power sensor was placed next to the objective. (c) Simulated dependence of trench depth on normalized input power under assumption of constant viscosity of the polymer film. (d) AFM images of trenches formed at different exposure wavelengths. (e) Trench depth profiles traced along the CNT axis. (f) Wavelength dependence of the trench area.

force terms (see Methods in the SI). In addition, we consider two-dimensional thermocapillary flows in a plane perpendicular to the CNT axis, since the laser beam diameter is much larger than the film thickness and the intensity gradient along the CNT axis can be regarded as negligible. Under this approximation, the trench depth directly above the CNT was adopted as the metric. The simulation results indicate a linear relationship between trench depth and input power delivered to the CNT assuming constant viscosity of the polymer film (Fig. 2c). Therefore, because the maximum laser power incident on the sample varies with wavelength in our optical setup (Fig. 2b), we calibrated the measured trench area using the laser power at 1200 nm. This procedure yields a quantity proportional to the optical absorption under the assumption of linear response.

Infrared trench spectroscopy of individual CNTs

Before conducting detailed spectroscopy on a CNT with a specific chirality, we first applied the trench-based method to multiple CNTs to evaluate whether variations in optical absorption could be observed among different nanotubes. The irradiation wavelengths were varied from 1200 to 1450 nm in 50 nm increments, and multiple trenches were formed above each CNT (Fig. S3). The trench areas, calibrated by the incident laser power, are presented in Fig. 3a. The number of trenches observed, and their calibrated areas differ among CNTs, with three to six trenches typically formed along a single CNT. These variations are attributed to chirality-dependent optical absorption characteristics. Notably, the trench areas show a consistent reduction near 1400 nm. This behaviour may indicate that the CNTs examined here possess relatively small diameters, resulting in comparatively weak optical absorption in this spectral region.

To extend trench formation over a broader wavelength range and under increased irradiation conditions, we prepared sufficiently long CNTs (Fig. 3b) and selected a CNT expected to exhibit broad near-infrared absorption based on the chirality assignment by Raman spectroscopy. The CNT highlighted by the red frame exhibited a radial breathing mode (RBM) peak and was tentatively assigned as a semiconducting (23,7) CNT

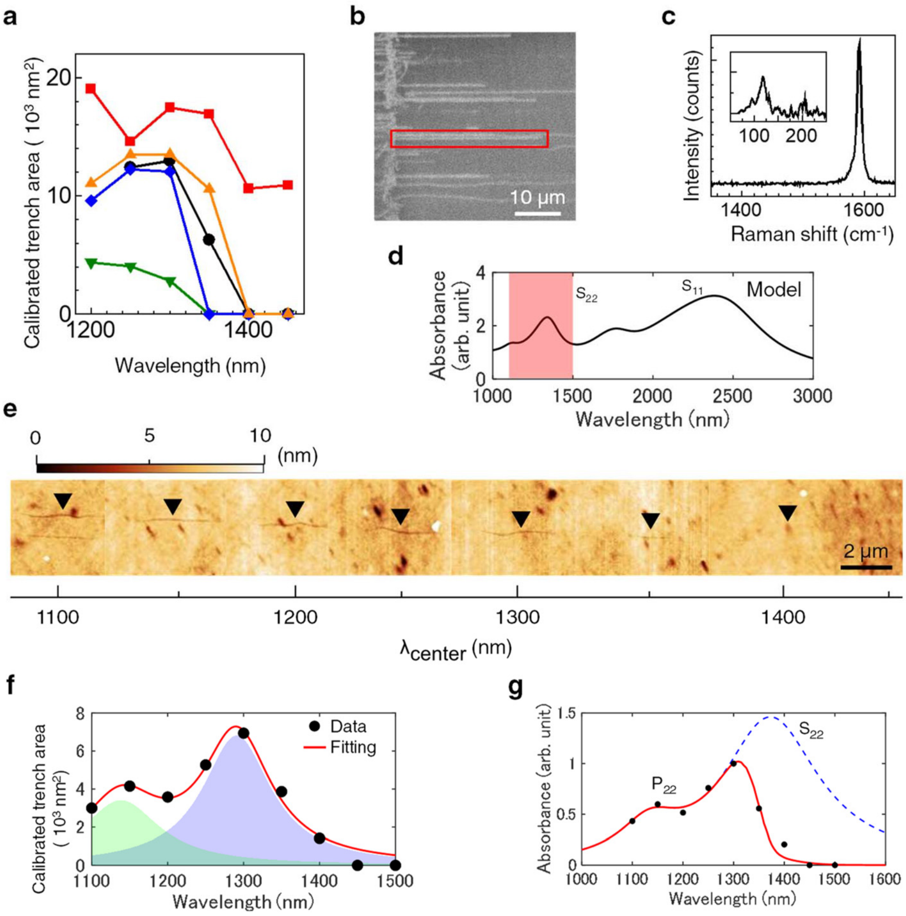

Fig. 3 (a) Trench area spectroscopy of multiple CNTs. (b, c) SEM image (b) of the CNT and the corresponding Raman spectrum (c) acquired from the same CNT. (d) Absorption spectrum of the (23,7) CNT empirically estimated based on a complex susceptibility model.[40] (e) AFM images of trenches formed on the CNT. The image is a composite of multiple images. (f) Wavelength dependence of the trench area after calibration by laser power (black dots) and the fitted curve (red). (g) Reconstructed absorption spectrum (blue dashed line) and the trench responsivity-weighted spectrum (red curve).

with a diameter of 2.16 nm (Fig. 3c, see Methods in the SI). The absorption spectrum of the (23,7) CNT was empirically estimated using a complex susceptibility model[40] (Fig. 3d). In this model, the complex susceptibility is represented as a sum of Lorentzian functions corresponding to excitonic transitions (S_{ii}) and phonon sidebands (P_{ii}) originating from longitudinal optical phonons, together with a background contribution. As parameter constraints, fitting data for the complex susceptibility of a (10,3) CNT were used, and the energy separation between P_{ii} and the corresponding S_{ii} was fixed to be 0.2 eV. The S_{ii} values were estimated by extrapolating photoluminescence excitation spectra of air-suspended CNTs wrapped with molecules from the air,[41] yielding S_{11} and S_{22} transition energies of 0.521 eV (2379.4 nm) and 0.937 eV (1323.3 nm), respectively (Fig. S5). Because the CNT in the present experiment is supported on a substrate, an overall redshift due to dielectric screening is anticipated. Nevertheless, the model is employed here for a qualitative comparison of spectral features rather than for a precise quantitative prediction.

Trench spectroscopy measurements were then performed by varying the irradiation wavelengths from 1100 to 1500 nm in 50 nm steps. The laser beam was scanned perpendicular to the CNT axis at a speed of 1 μm h^{-1}. To enhance thermocapillary flows, the sample was mounted on a heater maintained at 100 °C during irradiation. The CNT position was identified using metal alignment markers patterned on the substrate. Fig. 3e shows AFM images of trenches formed under different wavelength conditions. As described previously, the trench areas were calibrated by the incident laser power (Fig. 3f). The calibrated trench area increased from 1100 to 1300 nm, followed by a pronounced decrease, and no trench formation was observed at 1450 and 1500 nm. The experimental data were fitted with two Lorentzian functions, yielding peak energies of 1.089 eV (1138.5 nm) and 0.960 eV (1291 nm).

When the experimentally obtained trench areas are compared with the empirically estimated absorption shown in Fig. 3g, two notable discrepancies appear: (i) the separation between the two fitted peaks and (ii) the absence of continuum absorption above 1400 nm. If the observed peaks correspond to an excitonic transition and its phonon sideband, the extracted energy separation of 0.129 eV is considerably smaller than the established value of 0.2 eV for the separation between P_{ii} and S_{ii} transitions, which reflects the phonon energy involved in exciton–phonon coupling. In addition, no trench formation was detected at 1450 and 1500 nm, implying negligible optical absorption in this region. However, typical absorption spectra of CNTs exhibit a finite continuum absorption band[14] around 1500 nm between the S_{11} and S_{22} subband transitions, as illustrated in Fig. 3d. If the trench area were strictly proportional to the absorbed laser power, trench formation should persist in wavelength regions where the CNT exhibits finite absorption. The disappearance of trenches at longer wavelengths therefore suggests that the relationship between the absorbed power and trench area is not purely linear. Instead, it may involve nonlinear thermocapillary behaviour and the presence of a threshold power required for trench formation.

Thermofluidic simulation incorporating temperature-dependent viscosity

To clarify these discrepancies, we revisited the trench formation model. In the conventional description, the viscosity μ of the organic thin film is assumed to be constant and independent of temperature. Under this assumption, the trench depth increases linearly with the input power (Fig. 2c). In the present experiments, however, the sample was maintained at 100 °C, close to the glass transition temperature of PMMA, to enhance thermocapillary flows. Under these conditions, the additional local temperature rise induced by laser heating can significantly reduce the film viscosity, thereby altering the flow dynamics and trench formation process. To account for this effect, we modelled the PMMA viscosity as a temperature-dependent quantity $\mu(T_{\text{surface}})$,[42,43] and investigated how locally reduced viscosity under laser heating influences thermocapillary flows and trench formation (Fig. 4a–f).

Even when the time-averaged input power is fixed, the instantaneous viscosity of the film strongly depends on the temporal profile of the laser. Therefore, we examined trench formation under different duty ratios while maintaining a constant pulse width (2 ns) and time-averaged input power (Fig. 4a). The temperature distribution corresponding to a duty ratio of 0.2% (repetition rate of 1 MHz) is shown in Fig. 4b (top). Fig. 4c and d present the temporal evolution of the film surface temperature $T_{\text{surface}}(x)$ and the temperature at the film–substrate interface $T_{\text{bottom}}(0)$, respectively. When a point heat source is applied for 2 ns, the generated heat initially spreads laterally along the film bottom (Fig. 4d). At the film surface, however, the temperature increase is delayed due to finite thermal diffusion through the film thickness. As a result, $T_{\text{surface}}(0)$ reaches its maximum at approximately 3 ns and subsequently decays (Fig. 4c). The corresponding time-dependent change in film viscosity is shown in Fig. 4b (bottom). Owing to the transient rise in surface temperature, the viscosity of PMMA decreases to approximately 20% of its value at $T_{\text{surface}}(\infty)$. Incorporating this temperature-dependent viscosity into the trench formation model enables analysis of trench evolution under various irradiation conditions.

We first evaluated the dependence of trench depth on the duty ratio of the absorbed power. Fig. 4e shows the time evolution of trench depth for different duty ratios. The trench depth obtained at a duty ratio of 0.2% is significantly greater than that observed at a 2% duty ratio or under continuous-wave (CW) heating. We further analysed the dependence of trench formation rate on input power for pulsed and CW irradiation. As shown in Fig. 4f, the trench formation rate increases linearly with power under CW heating, whereas under pulsed heating it exhibits a superlinear dependence on power. This behaviour arises from the transient temperature spike during each pulse, which markedly reduces the film viscosity and thereby enhances thermocapillary flows in a nonlinear manner.

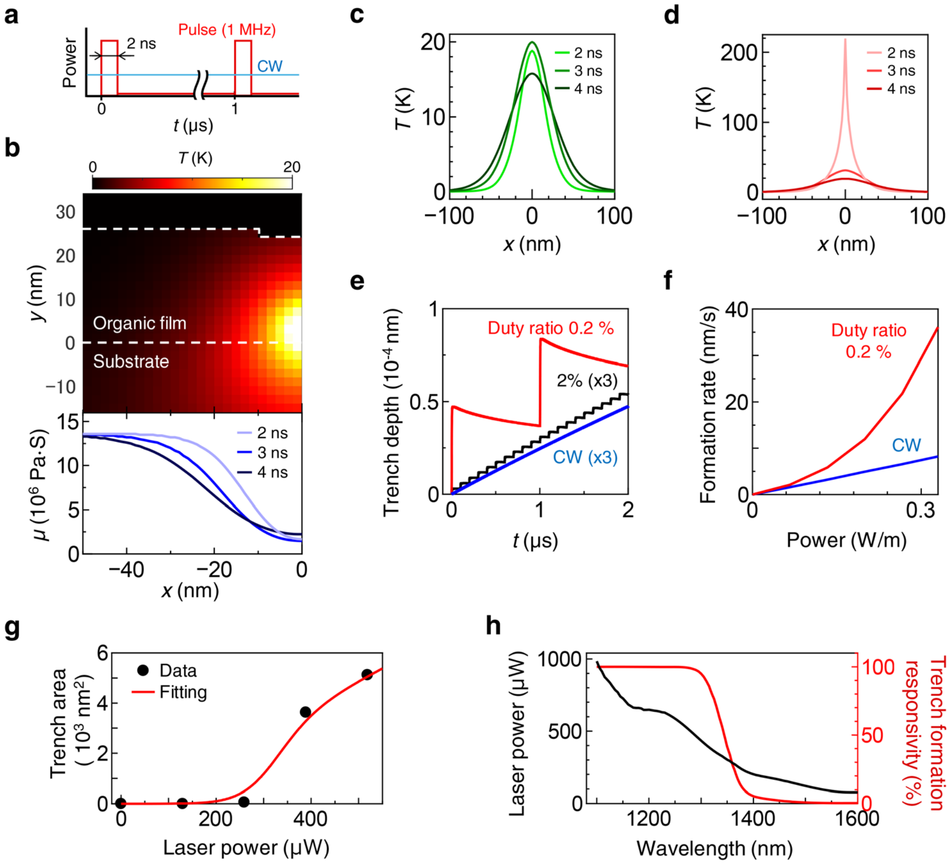

Fig. 4 (a) Schematic diagram of continuous wave (CW) and pulse heating. The pulse width and time-averaged power are fixed. (b) Two-dimensional temperature distribution in the thermofluidic simulation (top) and the temporal evolution of thin-film viscosity after irradiation with a 2 ns heat pulse (bottom). (c) Temporal evolution of the temperature at the film surface and (d) at the film bottom. (e) Time evolution of trench depth for different duty ratios. Data for the 2% duty ratio and CW conditions are scaled by a factor of three for clarity. (f) Simulated power dependence of the trench formation rate. (g) Experimentally obtained power dependence of trench area. (h) Wavelength dependence of the irradiation power and trench response rate.

Extraction of the intrinsic spectrum through nonlinear correction

To determine whether the nonlinear behaviour predicted by the simulations is also manifested experimentally, we conducted power-dependent measurements of the trench area. Trench formation was performed on a single CNT while varying the laser power along the tube axis, with the irradiation wavelength fixed at 1200 nm. The supercontinuum laser used in this experiment had a pulse width of 2 ns and a duty ratio of 0.004%. The measured power dependence of trench depth is presented in Fig. 4g. No trench was detected by AFM below an irradiation power of 300 μW. For higher powers, trenches were clearly formed, and the trench depth increased approximately linearly with power. These observations indicate the presence of a threshold absorbed power required for trench formation. Above this threshold, the trench area increases linearly with power. This threshold behavior is considered to originate from the temperature-dependent viscosity of the polymer film. Accordingly, the trench area A in the present system does not exhibit a purely linear dependence on laser power. Instead, we approximate the behaviour as $A \propto P \times S(P)$, where P denotes the laser power and $S(P)$ represents a sigmoid-like function describing the threshold response. As shown in Fig. 2b, the maximum irradiation power $P(\lambda)$ incident on the samples depends on the centre wavelength. Therefore, the measured trench area reflects not only the intrinsic optical absorption of the CNT but also the wavelength-dependent responsivity of the trench formation process.

To obtain an intrinsic spectrum, it is thus necessary to evaluate the wavelength dependence of the trench responsivity associated with power attenuation in the optical system. Fig. 4h shows the calculated trench responsivity corresponding to the reduction in trench area at longer wavelengths. The responsivity begins to decrease at approximately 1300 nm and approaches zero at approximately 1550 nm, indicating a spectral region where trench formation no longer occurs. These results demonstrate that, in addition to power calibration, a correction for responsivity is essential for accurate spectral analysis. It is noteworthy that the trench depth profile along the CNT in Fig. 2e reflects the spatial intensity distribution of the laser at the sample surface. In several cases, the trench depth profile along the tube axis was narrower than the incident beam profile, suggesting that the nonlinear threshold response is embedded within an individual trench profile (Fig. S4). This spatial confinement implies the possibility of sub-diffraction-limited thermal patterning based on the nonlinearity.

By correcting for the nonlinear response originating from thermocapillary flows, the intrinsic optical absorption spectrum of the CNT can be estimated from the measured trench areas. The trench area variation shown in Fig. 3f was reanalysed using an absorption model based on the complex susceptibility of the CNT, multiplied by the calculated trench responsivity. The model assumed two Lorentzian functions corresponding to S_{22} and P_{22} separated by 0.2 eV, together with a featureless continuum band. As shown in Fig. 3g, the S_{22} absorption peak was found at 0.903 eV (1372 nm), while the corresponding phonon sideband (P_{22}) appeared at 1.074 eV (1154 nm). Compared with the S_{22} transition energy of 0.937 eV (1323.3 nm) estimated from the extrapolation of values reported for air-suspended CNTs wrapped with molecules from the air, the observed peak exhibits a redshift of approximately 34 meV. This shift is attributed to dielectric screening effects induced by the quartz substrate. The magnitude of the redshift is consistent with previously reported values[28,30] and is therefore considered physically reasonable. The strain effect induced by the quartz substrate is suggested to have been relieved during the sample fabrication process.[19] These results demonstrate that incorporating trench responsivity into the analysis enables extraction of intrinsic absorption features of an individual CNT from the nonlinear thermocapillary response.

Conclusions

We developed a spectroscopic method based on laser-induced nanoscale thermocapillary flows and demonstrated infrared absorption measurements of an individual CNT. By interpreting the trench formed on the surface of an organic thin film as a thermal imprint of CNT optical absorption, we quantitatively evaluated the wavelength dependence of light absorption. Trench spectroscopy conducted over the 1100–1500 nm range enabled the reconstruction of the excitonic transition (S_{22}) and the associated phonon sideband (P_{22}) for an individual CNT. Thermofluidic simulations incorporating the temperature dependence of film viscosity revealed that pulsed laser irradiation induces nonlinear amplification of the trench formation rate. The nonlinearity-corrected trench spectroscopy method established in this work provides a practical route toward bandgap-level selectivity in CNT purification, enabling diameter-selective purification under identical processing conditions. Beyond CNTs, the insights into nanoscale thermocapillary dynamics obtained here not only provide a quantitative photothermal approach for characterizing heterogeneous low-dimensional nanomaterials but also offer a basis for advancing high-resolution thermal lithography.

Experimental section

Growth of horizontally aligned SWCNTs

Iron was employed as the catalyst for the growth of horizontally aligned CNTs. Catalyst lines were patterned on an ST-cut single-crystalline α-quartz substrate (University Wafer, Inc.) using photolithography. ST-cut quartz was employed because it is a standard substrate for the growth of horizontally aligned single-walled CNTs. A nominal 0.08 nm thick iron layer was deposited by thermal evaporation, leading to the formation of catalyst nanoparticles. CNTs were synthesized by alcohol catalytic chemical vapor deposition (ACCVD). Prior to growth, the iron catalyst was reduced in an Ar/H_2 atmosphere (40 kPa) at 800 °C for 10 min. CNT growth was subsequently conducted at 800 °C for 1 h under a total pressure of 660 Pa using C_2H_5OH (5 sccm) as the carbon source and Ar/H_2 (50 sccm). Raman spectroscopy and mapping measurements were performed with a home-made system using an excitation wavelength of 532 nm.[44]

Thin-film deposition

A 1 wt% PMMA solution was prepared by diluting a 4 wt% stock solution. PMMA powder was dissolved in anisole and maintained at 80 °C overnight to ensure complete dissolution. Additional anisole was then added to adjust the concentration to 1 wt%. PMMA thin films were deposited by spin coating. The solution was first spread at 100 rpm for 15 s, followed by acceleration for 5 s and spinning at 4000 rpm for 60 s.

Optical setup and trench formation

Trench-based spectroscopy was carried out using a white laser source (SuperK COMPACT, NKT Photonics). The irradiation wavelength was selected with a tunable bandpass filtering system composed of a long-pass filter (FELHV2, Thorlabs, Inc.) and a short-pass filter (FESHV2, Thorlabs, Inc.), yielding a bandwidth of 50 nm. The filtered laser beam was focused onto the sample through a 50× objective lens. The laser polarization was aligned parallel to the CNT axis using a polarizing beam splitter to maximize absorption. The focal position was automatically optimized by monitoring the reflected light from the substrate surface in a confocal manner when the irradiation wavelength was changed to minimize the fluctuations of laser power density. The laser power was measured by power sensor (S122C, Thorlabs, Inc.) placed next to the objective.

Author contributions

Kai Watanabe: writing – original draft, methodology, investigation, data curation, formal analysis, visualization. Shigeo Maruyama: writing – review & editing, funding acquisition. Keigo Otsuka: writing – review & editing, conceptualization, methodology, validation, project administration, supervision, funding acquisition.

Conflicts of interest

There are no conflicts to declare.

Data availability

The data supporting this article are available within the article and its supplementary information (SI). Supplementary information: AFM images, raw transmission spectra of the experiment setup, methods of prediction about excitonic transition energies and the thermofluidic simulation. See DOI: https://doi.org/10.1039/d6nr00807k.

Additional datasets generated and analysed during the current study are available from the corresponding author upon reasonable request.

Acknowledgements

Part of this work is supported by JSPS (KAKENHI JP22H01411, JP23K22682, JP23H05443 and JP26K00883) and JST (CREST JPMJCR20B5), the Ministry of Education, Culture, Sports, Science and Technology (MEXT), Japan. Part of this work was supported by "Advanced Research Infrastructure for Materials and Nanotechnology in Japan" of the Ministry of Education, Culture, Sports, Science and Technology (MEXT), Grant Number JPMXP1225UT1109, and fabrication was conducted in Takeda Cleanroom with help of Nanofabrication Platform Center of School of Engineering, the University of Tokyo, Japan. This study was partly supported by the World-leading Innovative Graduate Study Program in Proactive Environmental Studies (WINGS-PES), The University of Tokyo.

References

1 S. T. Howell, A. Grushina, F. Holzner and J. Brugger, Thermal scanning probe lithography—a review, *Microsyst. Nanoeng.*, 2020, **6**, 21.

2 A. Y. Zykov and N. A. Ivanova, Laser-induced thermocapillary convection in thin liquid layers: effect of thermal conductivity of substrates, *Appl. Phys. B*, 2017, **123**, 235.

3 O. A. Tarasov, Evaluation of the possibility of using the laser-induced thermocapillary effect for photothermal spectroscopy, *Opt. Spectrosc.*, 2005, **99**, 968.

4 M. R. Rosenberger, M. C. Wang, X. Xie, J. A. Rogers, S. Nam and W. P. King, Measuring individual carbon nanotubes and single graphene sheets using atomic force microscope infrared spectroscopy, *Nanotechnology*, 2017, **28**, 355707.

5 H. Hu, H. Cho, S. Somnath, A. F. Vakakis and W. P. King, Silicon nano-mechanical resonators fabricated by using tip-based nanofabrication, *Nanotechnology*, 2014, **25**, 275301.

6 F. Xiong, A. D. Liao, D. Estrada and E. Pop, Low-Power Switching of Phase-Change Materials with Carbon Nanotube Electrodes, *Science*, 2011, **332**, 568.

7 X. Zheng, A. Calò, E. Albisetti, X. Liu, A. S. M. Alharbi, G. Arefe, X. Liu, M. Spieser, W. J. Yoo, *et al.*, Patterning metal contacts on monolayer MoS2 with vanishing Schottky barriers using thermal nanolithography, *Nat. Electron.*, 2019, **2**, 17.

8 S. H. Jin, S. N. Dunham, J. Song, X. Xie, J. H. Kim, C. Lu, A. Islam, F. Du, J. Kim, *et al.*, Using nanoscale thermocapillary flows to create arrays of purely semiconducting single-walled carbon nanotubes, *Nat. Nanotechnol.*, 2013, **8**, 347.

9 X. Xie, S. H. Jin, M. A. Wahab, A. E. Islam, C. Zhang, F. Du, E. Seabron, T. Lu, S. N. Dunham, *et al.*, Microwave purification of large-area horizontally aligned arrays of single-walled carbon nanotubes, *Nat. Commun.*, 2014, **5**, 5332.

10 F. Du, J. R. Felts, X. Xie, J. Song, Y. Li, M. R. Rosenberger, A. E. Islam, S. H. Jin, S. N. Dunham, C. Zhang, W. L. Wilson, Y. Huang, W. P. King and J. A. Rogers, Laser-Induced Nanoscale Thermocapillary Flow for Purification of Aligned Arrays of Single-Walled Carbon Nanotubes, *ACS Nano*, 2014, **8**, 12641.

11 M. Ichida, S. Saito, T. Nakano, Y. Feng, Y. Miyata, K. Yanagi, H. Kataura and H. Ando, Absorption spectra of high purity metallic and semiconducting single-walled carbon nanotube thin films in a wide energy region, *Solid State Commun.*, 2011, **151**, 1696.

12 H. Kataura, Y. Kumazawa, Y. Maniwa, I. Umezu, S. Suzuki, Y. Ohtsuka and Y. Achiba, Optical properties of single-wall carbon nanotubes, *Synth. Met.*, 1999, **103**, 2555.

13 Y. Miyauchi and S. Maruyama, Identification of an excitonic phonon sideband by photoluminescence spectroscopy of single-walled carbon-13 nanotubes, *Phys. Rev. B:Condens. Matter Mater. Phys.*, 2006, **74**, 035415.

14 S. Dal Forno, N. Komatsu, M. Wais, A. Mojibpour, I. Wadgaonkar, S. Ghosh, Y. Yomogida, K. Yanagi, K. Held, J. Kono and M. Battiato, Origin of the background absorption in carbon nanotubes: Phonon-assisted excitonic continuum, *Carbon*, 2022, **186**, 465.

15 K. Liu, J. Deslippe, F. Xiao, R. B. Capaz, X. Hong, S. Aloni, A. Zettl, W. Wang, X. Bai, S. G. Louie, E. Wang and F. Wang, An atlas of carbon nanotube optical transitions, *Nat. Nanotechnol.*, 2012, **7**, 325.

16 F. Yao, C. Liu, C. Chen, S. Zhang, Q. Zhao, F. Xiao, M. Wu, J. Li, P. Gao, J. Zhao, X. Bai, S. Maruyama, D. Yu, E. Wang, Z. Sun, J. Zhang, F. Wang and K. Liu, Measurement of complex optical susceptibility for individual carbon nanotubes by elliptically polarized light excitation, *Nat. Commun.*, 2018, **9**, 3387.

17 R. Dong, J. Bi, S. Sun, Z. Zhou, Q. Lin, T. Hao, K. Watanabe, T. Taniguchi, M. Wang, J. Jiang, H. Wu and S. Zhao, Extended Kataura plot of single-walled carbon nanotubes and on-demand fabrication of mixed-dimensional heterostructures, *Carbon*, 2024, **230**, 119610.

18 K. Yanagi, R. Moriya, Y. Yomogida, T. Takenobu, Y. Naitoh, T. Ishida, H. Kataura, K. Matsuda and Y. Maniwa, Electrochromic Carbon Electrodes: Controllable Visible Color Changes in Metallic Single–Wall Carbon Nanotubes, *Adv. Mater.*, 2011, **23**, 2811.

19 T. Ozel, D. Abdula, E. Hwang and M. Shim, Nonuniform Compressive Strain in Horizontally Aligned Single-Walled Carbon Nanotubes Grown on Single Crystal Quartz, *ACS Nano*, 2009, **3**, 2217.

20 W. Yang, R.-Z. Wang and H. Yan, Strain-induced Raman-mode shift in single-wall carbon nanotubes: Calculation of force constants from molecular-dynamics simulations, *Phys. Rev. B:Condens. Matter Mater. Phys.*, 2008, **77**, 195440.

21 Z. Liu, J. Zhang and B. Gao, Raman spectroscopy of strained single-walled carbon nanotubes, *Chem. Commun.*, 2009, 6902.

22 T. K. Leeuw, D. A. Tsyboulski, P. N. Nikolaev, S. M. Bachilo, S. Arepalli and R. B. Weisman, Strain measurements on individual single-walled carbon nanotubes in a polymer host: Structure-dependent spectral shifts and load transfer, *Nano Lett.*, 2008, **8**, 826.

23 M. Rohlfing, Redshift of Excitons in Carbon Nanotubes Caused by the Environment Polarizability, *Phys. Rev. Lett.*, 2012, **108**, 087402.

24 F. Wang, M. Y. Sfeir, L. Huang, X. M. H. Huang, Y. Wu, J. Kim, J. Hone, S. O'Brien, L. E. Brus and T. F. Heinz, Interactions between Individual Carbon Nanotubes Studied by Rayleigh Scattering Spectroscopy, *Phys. Rev. Lett.*, 2006, **96**, 167401.

25 O. A. Dyatlova, J. Gomis-Bresco, E. Malic, H. Telg, J. Maultzsch, G. Zhong, J. Geng and U. Woggon, Dielectric screening effects on transition energies in aligned carbon nanotubes, *Phys. Rev. B:Condens. Matter Mater. Phys.*, 2012, **85**, 245449.

26 Y. Miyauchi, R. Saito, K. Sato, Y. Ohno, S. Iwasaki, T. Mizutani, J. Jiang and S. Maruyama, Dependence of exciton transition energy of single-walled carbon nanotubes on surrounding dielectric materials, *Chem. Phys. Lett.*, 2007, **442**, 394.

27 T. Ando, Effects of environmental dielectric screening on optical absorption in carbon nanotubes, *Phys. E*, 2011, **43**, 798.

28 M. Steiner, M. Freitag, J. C. Tsang, V. Perebeinos, A. A. Bol, A. V. Failla and P. Avouris, How does the substrate affect the Raman and excited state spectra of a carbon nanotube?, *Appl. Phys. A*, 2009, **96**, 271.

29 Y. Ohno, S. Iwasaki, Y. Murakami, S. Kishimoto, S. Maruyama and T. Mizutani, Excitonic transition energies in single–walled carbon nanotubes: Dependence on environmental dielectric constant, *Phys. Status Solidi B*, 2007, **244**, 4002.

30 A. G. Walsh, A. N. Vamivakas, Y. Yin, S. B. Cronin, M. S. Ünlü, B. B. Goldberg and A. K. Swan, Screening of Excitons in Single, Suspended Carbon Nanotubes, *Nano Lett.*, 2007, **7**, 1485.

31 L. Aspitarte, D. R. McCulley, A. Bertoni, J. O. Island, M. Ostermann, M. Rontani, G. A. Steele and E. D. Minot, Giant modulation of the electronic band gap of carbon nanotubes by dielectric screening, *Sci. Rep.*, 2017, **7**, 8828.

32 C. A. Silvera-Batista, R. K. Wang, P. Weinberg and K. J. Ziegler, Solvatochromic shifts of single-walled carbon nanotubes in nonpolar microenvironments, *Phys. Chem. Chem. Phys.*, 2010, **12**, 6990.

33 J. H. Choi and M. S. Strano, Solvatochromism in single-walled carbon nanotubes, *Appl. Phys. Lett.*, 2007, **90**, 223114.

34 P. Finnie, Y. Homma and J. Lefebvre, Band-Gap Shift Transition in the Photoluminescence of Single-Walled Carbon Nanotubes, *Phys. Rev. Lett.*, 2005, **94**, 247401.

35 Y. Homma, S. Chiashi, T. Yamamoto, K. Kono, D. Matsumoto, J. Shitaba and S. Sato, Photoluminescence Measurements and Molecular Dynamics Simulations of Water Adsorption on the Hydrophobic Surface of a Carbon Nanotube in Water Vapor, *Phys. Rev. Lett.*, 2013, **110**, 157402.

36 T. Hertel, A. Hagen, V. Talalaev, K. Arnold, F. Hennrich, M. Kappes, S. Rosenthal, J. McBride, H. Ulbricht and E. Flahaut, Spectroscopy of single- and double-wall carbon nanotubes in different environments, *Nano Lett.*, 2005, **5**, 511.

37 H. Huang, D. Zhang, N. Wei, S. Wang and L. Peng, Plasmon–Induced Enhancement of Infrared Detection Using a Carbon Nanotube Diode, *Adv. Opt. Mater.*, 2017, **5**, 1600865.

38 K. Liu, X. Hong, Q. Zhou, C. Jin, J. Li, W. Zhou, J. Liu, E. Wang, A. Zettl and F. Wang, High-throughput optical imaging and spectroscopy of individual carbon nanotubes in devices, *Nat. Nanotechnol.*, 2013, **8**, 917.

39 J. Song, C. Lu, C. Zhang, S. H. Jin, Y. Li, S. N. Dunham, X. Xie, F. Du, Y. Huang and J. A. Rogers, Modeling of thermocapillary flow to purify single-walled carbon nanotubes, *RSC Adv.*, 2014, **4**, 42454.

40 T. Nishihara, A. Takakura, M. Shimasaki, K. Matsuda, T. Tanaka, H. Kataura and Y. Miyauchi, Empirical formulation of broadband complex refractive index spectra of single-chirality carbon nanotube assembly, *Nanophotonics*, 2022, **11**, 1011.

41 A. Ishii, M. Yoshida and Y. K. Kato, Exciton diffusion, end quenching, and exciton-exciton annihilation in individual air-suspended carbon nanotubes, *Phys. Rev. B:Condens. Matter Mater. Phys.*, 2015, **91**, 125427.

42 F. Sidorov and A. Rogozhin, Thermal Reflow Simulation for PMMA Structures with Nonuniform Viscosity Profile, *Polymers*, 2023, **15**, 3731.

43 S. H. Jin, J. Song, H. U. Chung, C. Zhang, S. N. Dunham, X. Xie, F. Du, T. Kim, J.-H. Lee, Y. Huang and J. A. Rogers, Fundamental effects in nanoscale thermocapillary flow, *J. Appl. Phys.*, 2014, **115**, 054315.

44 K. Otsuka and S. Maruyama, Catalyst-mediated etching of carbon nanotubes exhibiting electronic-structure insensitivity and reciprocal kinetics with growth, *Carbon*, 2025, **243**, 120530.